# Scaled interfacial length in partially miscible Saffman-Taylor instability: Experimental demonstration of gap and flow rate effects

Ryuta X. Suzuki [1,2,3,*] Yusuke Nabae [4] and Hiroya Mamori [5]

[1] *Department of Applied Physics and Chemical Engineering, Tokyo University of Agriculture and Technology, Nakacho 2-24-16, Koganei, Tokyo 184–8588, Japan*

[2] *West Tokyo Joint Center for Sustainability Research and Implementation, Nakacho 2-24-16, Koganei, Tokyo 184–8588, Japan*

[3] *PRESTO, Japan Science and Technology Agency, Kawaguchi, Saitama 332-0012, Japan*

[4] *Department of Mechanical Engineering, Tokyo University of Science, 6-3-1 Niijuku, Katsushika-ku, Tokyo 125–8585, Japan*

[5] *Department of Mechanical and Intelligent Systems Engineering, The University of Electro-Communications, 1-5-1, Chofugaoka, Chofu, Tokyo 182–8585, Japan*

(Received 15 October 2025; accepted 15 December 2025; published 26 January 2026)

Fluid displacement in porous media is a key process in many industrial and environmental applications. When a less viscous fluid displaces a more viscous one in porous media or Hele-Shaw cells, a finger-like interfacial pattern known as the Saffman-Taylor instability typically occurs. Recently, partially miscible systems have attracted attention because they exhibit multiple droplet formations instead of conventional fingering. While the effects of Hele-Shaw-cell gap width on hydrodynamic instability have been well established in fully miscible and immiscible systems, where narrower gaps produce thinner and more numerous fingers, the influence of gap confinement in partially miscible systems remains unclear. In this study, we experimentally investigated the effect of gap width on fluid displacement dynamics in a partially miscible PEG-$Na_2SO_4$-water system. The droplet size decreased and the number of the droplets increased as the gap became smaller, indicating that confinement intensified droplet formation. The total interfacial length was successfully scaled using the flow rate, flow velocity, and gap width, collapsing onto a universal curve when expressed as a function of flow-rate-to-gap ratio. The derived empirical exponent was consistent with a force balance between inertial and capillary stresses, suggesting a transitional "inertia-modified capillary" regime. This scaling framework provides predictive insights into the interfacial morphology of partially miscible systems, bridging thermodynamic interfacial forces and hydrodynamic flow.

DOI: 10.1103/qcgd-hd4v

## I. INTRODUCTION

The Saffman-Taylor instability [1] or viscous fingering (VF) [2,3] produces a finger-like interfacial pattern when a more viscous fluid is displaced by a less viscous fluid in porous media or in Hele-Shaw cells. Hele-Shaw cells, which consist of a thin gap between two parallel plates [4], are frequently used instead of porous media because the governing flow equation in Hele-Shaw cells is identical to that in porous media [5].

VFs are classified into two categories: fully miscible and immiscible. A fully miscible system has infinite mutual solubility, meaning the two fluids are completely soluble in each other, and diffusion

*Contact author: ryuta.x.suzuki@gmail.com

 

plays a key role in this system. By contrast, an immiscible system exhibits zero mutual solubility, where the two fluids do not dissolve in each other; thus, the composition of the initial solutions remains unchanged over time. In this system, interfacial tension is critical. The fingers in immiscible systems are wider than those in fully miscible systems because of interfacial tension [3]. Studying VF is important for several environmental and industrial processes, such as chromatography [6], digestive fluid transport [7], frontal polymerization [8] and oil recovery [9].

The effect of the gap width in Hele-Shaw cells on VF dynamics has been extensively investigated in recent studies [10–14]. Al-Housseiny *et al*. experimentally [10] and theoretically [11] examined the control of immiscible VFs using a geometric strategy in which the Hele-Shaw cell had a constant depth gradient along the flow direction. Zheng *et al*. [12] experimentally and theoretically suppressed immiscible fingering dynamics using a time-dependent gap strategy, where the gap width of the Hele-Shaw cells varied with $t^{1/7}$ ($t$ represents time). Bongrand and Tsai [13] experimentally demonstrated the complete displacement of more viscous oil by less viscous air in radial Hele-Shaw cells with a fixed gap gradient. They investigated the stability of VF patterns by varying the gap gradient and injection flow rate, and compared their experimental results with linear stability theory, showing that the critical threshold capillary number increased with the gap gradient, which is in good agreement with the theoretical prediction. Nand *et al*. [14] experimentally and numerically revealed that the gap width affects fully miscible VFs. They observed that increasing the gap width suppressed VF instability for a fixed mobility ratio and flow rate. In both classical theory and this study, instability increased with the Péclet number (Pe), defined as the ratio of advection rate to diffusion rate. However, even at a fixed Pe, the instability weakens as the gap widens, indicating a gap effect on instability. They also simulated VF dynamics with different gap widths using comsol software, employing Darcy's law for two-dimensional flow and the Stokes model for three-dimensional flow. The Darcy model qualitatively reproduced the experimental results.

The effect of the gap, such as throat width and porosity, on VF dynamics in porous media has also been studied. The definition of "gap" in porous media varies among research groups. In some cases, it corresponds to the average throat width, while in others it represents the porosity. The governing equations of flow in Hele-Shaw cells and porous media are equivalent only when permeability is homogenous in the porous medium.

Wang *et al*. [15] numerically examined the effects of porosity and wettability on immiscible VF dynamics in porous media. By varying these parameters, they constructed a phase diagram of morphologies, including viscous fingering, capillary-fingering-like patterns, and suppressed instability. Pak *et al*. [16] numerically investigated how morphology changes, such as erosion and dilation of particles in porous media, influence immiscible fluid displacement dynamics. They modified both the porosity and throat width, observing that the wide-throat model contained larger oil clusters, whereas the tighter (dilated) model contained smaller clusters. Osei-Bonsu *et al*. [17] experimentally investigated the effects of pore throat size (i.e., porosity or permeability) on immiscible fluid displacement dynamics with foam production. They found that changes in permeability did not affect displacement efficiency. Heterogeneity also plays a significant role in fluid displacement dynamics in porous media [18–21].

A third VF category, the partially miscible system, has been recently studied [22–34]. Several definitions for partially miscible systems currently exist. In one definition, two solutions are brought into contact and one component from one solution diffuses into the other [22,23,27]. In another, both solutions mutually dissolve [28], so that the compositions of the initial solutions differed from those at later stages because phase separation occurs at the interface. In both cases, the solutions in the partially miscible system exhibit finite mutual solubility. The present study focuses on the latter case.

Partially miscible VFs produce multiple droplet formations instead of a finger-like patterns due to phase separation and spontaneous convection during phase separation [28]. The convection arises from the Korteweg force [35–40], which is driven by a chemical potential gradient across the interface between fluids of increasing viscosity. Experimental studies have focused on the effects of components, including the degree of partial miscibility or degree of phase separation,

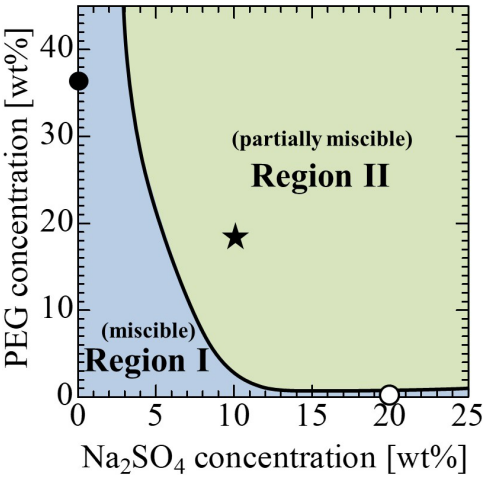


FIG. 1. Phase diagram of the PEG-$Na_2SO_4$-water system used in this study. The black solid circle indicates the concentration of 36.5 wt % PEG solution and white solid circle implies 20 wt % $Na_2SO_4$ solution. These solutions are brought into contact with each other, resulting in the concentration shown in a black star. The black solid curve indicates a so-called binodal curve.

injection flow rate, and mobility (such as viscosity contrast between fluids) on partially miscible displacement dynamics [26,28–30,32,34]. However, the influence of the Hele-Shaw gap width on partially miscible systems has not yet been investigated, even though it strongly affects droplet formation dynamics.

Therefore, this study experimentally investigates the effect of the Hele-Shaw gap width on VF dynamics, as well as the influence of injection flow rate and flow velocity. Displacement experiments were performed using partially miscible PEG-$Na_2SO_4$-water solutions under ambient conditions to systematically examine how geometric confinement and flow parameters affect interfacial behavior. The evolution of fingering and droplet formation was recorded and analyzed to clarify the mechanisms governing instability development in partially miscible fluid displacement.

## II. METHODS

A partially miscible system was prepared using polyethylene glycol (PEG; average molecular weight, $M_w = 8000$), $Na_2SO_4$, and water at room temperature and atmospheric pressure [41]. Figure 1 shows the phase diagram of the PEG-$Na_2SO_4$-water system. The solution composition used in this study was identical to that used in previous work [28].

When the initial concentrations of the displacing and displaced liquids lie within Region II (Fig. 1), the system is partially miscible, as it separates with finite mutual solubility. By contrast, when the initial concentration lies within Region I, the system forms a single phase, indicating a fully miscible system in which the fluids completely mix into a homogenous phase over time. The boundary curve between Regions I and II is referred to as the binodal curve.

The initial concentration was varied by changing the $Na_2SO_4$ concentration, while maintaining the more viscous liquid as a 36.5 wt % PEG solution, dyed with 0.1 wt % indigo carmine for displacement visualization. Although the $Na_2SO_4$ concentration was altered, the solution viscosity remained nearly constant. For instance, when the displaced liquid was 36.5 wt % PEG-63.5 wt % water [black solid circle (•) in Fig. 1] and the displacing liquid was 20 wt % $Na_2SO_4$-80 wt % water [open circle (◯) in Fig. 1], the mixture composition became 18.25 wt % PEG-10 wt % $Na_2SO_4$-71.75 wt % water [black star (⋆) in Fig. 1]. This composition was considered to represent the interfacial composition during fluid displacement. Moreover, because this composition lies on

TABLE I. Symbols and their definitions in this study.

| Symbol | Definition | Physical meaning | Unit |
|---|---|---|---|
| $b$ | Gap width of Hele–Shaw cell | Controls confinement; affects hydrodynamic instability | mm |
| $q$ | Flow rate | Injected fluid volume per unit time | $\mu$L min$^{-1}$ |
| $v$ | Flow velocity ($= q/b$) | Linear velocity | $\mu$L min$^{-1}$ mm$^{-1}$ |
| $f$ | Flow velocity ratio | Nondimensional flow length | |
| $D$ | Fractal dimension | Describes interfacial complexity | |
| $S$ | Randomness | Quantifies instability strength | |
| $I$ | Total interfacial length | Thermodynamic measure of interface development | mm |

the binodal curve in Fig. 1 (Region II), the system, where 36.5 wt % PEG was displaced by 20 wt % $Na_2SO_4$, underwent phase separation, confirming that it was partially miscible.

Previous studies have confirmed that all solutions used here behaved as Newtonian fluids [28,42,43]. In our previous study [43], the viscosity and density of each solution was measured and reported as follows: 36.5 wt % PEG had a 112 mPa s viscosity and 1.07 g cm$^3$ density, while 20 wt % $Na_2SO_4$ had a 2.08 mPa s viscosity and 1.19 g cm$^{-3}$ density.

Table I summarizes the symbols and corresponding definitions used in this study. In particular, the linear velocity ($v$) is defined as $q/b$ because a fixed representative radius ($r$) was used. The exact expression for the linear velocity is $q/(2\pi\, rb)$. In radial Hele-Shaw flow, the physically relevant characteristic velocity at the advancing front is the Darcy-type gap-averaged velocity $u_r = \frac{q}{2\pi rb}$, which has the correct units of $[L/T]$. Strictly speaking, the quantity $q/b$ is therefore a flux-like parameter rather than a true velocity. In this study, however, we use $v = q/b$ as a convenient flow-rate-based control parameter because, in the range of radii relevant to the fingering dynamics, the factor $2\pi r$ varies only weakly between experiments, making $u_r$ approximately proportional to $q/b$. Thus, $v$ should be interpreted as a hydrodynamic forcing parameter proportional to the Darcy velocity rather than as the exact local velocity field.

Displacement experiments were conducted using Hele-Shaw cells with various gap widths (0.05, 0.10, 0.15, 0.20, 0.25, 0.30, 0.35, 0.40, 0.50, 0.60, and 0.70 mm) (Fig. 2). The cells consist of two parallel acrylic plates. The size of the cells is 14×14 cm and the recorded diameter of the cells is 116 mm. The gap is controlled by the thickness of metal plates.

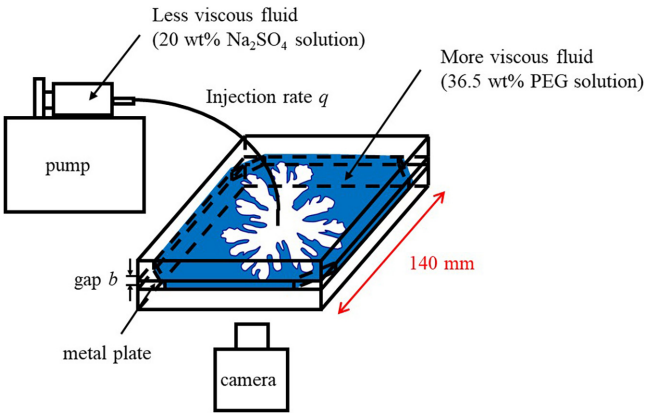


FIG. 2. Schematic of the fluid displacement apparatus.

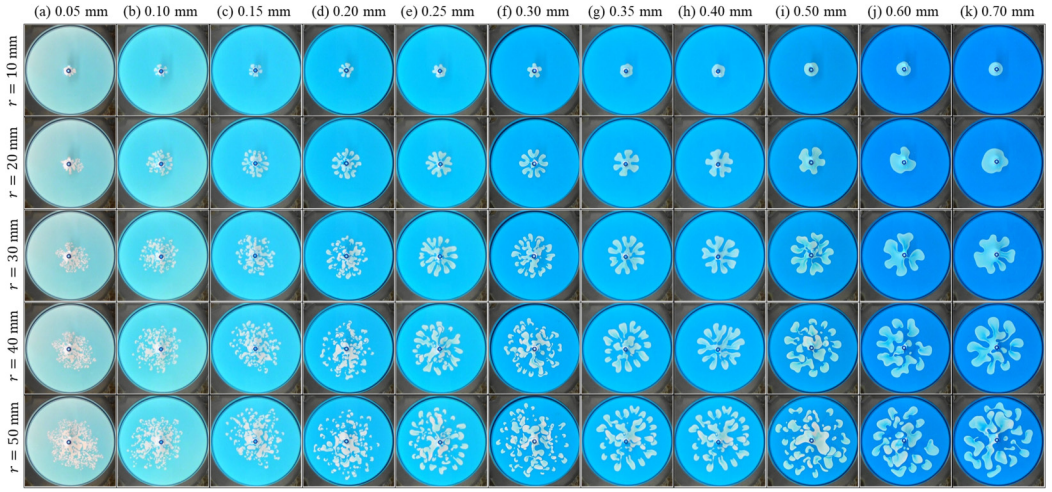


FIG. 3. Time evolution of fingering dynamics at various gap widths. From left to right, the gap width was (a) 0.05, (b) 0.10, (c) 0.15, (d) 0.20, (e) 0.25, (f) 0.30, (g) 0.35, (h) 0.40, (i) 0.50, (j) 0.60, and (k) 0.70 mm. From top to bottom, the image was taken when the radius of the longest finger or outermost droplet reached 10, 20, 30, 40, and 50 mm. The linear flow velocity ($q/b$) was fixed at 186 $\mu L\,min^{-1}\,mm^{-1}$.

The more viscous 36.5 wt % PEG solution was first used to fill the cell, followed by injection of the less viscous 20 wt % $Na_2SO_4$ solution at controlled flow rates (9.3–1302 $\mu L\,min^{-1}$), depending on the gap width, to maintain a constant reference linear flow velocity of 186 $\mu L\,min^{-1}\,mm^{-1}$. Additional experiments were performed at higher velocities of $2v_0$, $5v_0$, and $10v_0$ (372, 930, and 1860 $\mu L\,min^{-1}\,mm^{-1}$, respectively) to study the effect of flow velocity. Each experiment continued until the outermost finger or droplet reached a radial distance of 50 mm. The displacement processes were recorded from below using a video camera. To obtain quantitative data such as droplet count and average size, the images were first converted to grayscale and binarized using imagej. For complex patterns, the interfaces were manually traced on paper, scanned, and converted into binary images. The number and size of droplets were then measured using imagej software. Each experimental condition was repeated three times to ensure reproducibility, and the error bars in the figures represent standard deviations. In addition, we showed that the resolution of the camera used in this study was sufficiently high to analyze the displacement. The resolution of the camera is 1920 $\times$ 1080 pixels. The length of one image pixel in a 20 wt % $Na_2SO_4$ case is calculated to be 0.08369 mm. Hence, the area of 1 pixel was $0.08369^2\ mm^2 = 0.00700\ mm^2$. However, the average droplet size excluding a mother finger for Fig. 3(b) (shown later) was 6.319 $mm^2$. This value corresponded to 902 pixels. Thus, noise had little effect on the results of this study because the droplets occupied a sufficient pixel size.

## III. RESULTS AND DISCUSSION

Figure 3 shows the time evolution of the displacement when the 36.5 wt % PEG solution was displaced by a 20 wt % $Na_2SO_4$ solution at various gap widths. The flow rate was adjusted so that the flow velocity remained constant at 186 $\mu L\,min^{-1}\,mm^{-1}$) for all gaps. For example, when the gap was 0.05 mm, the flow rate was $186 \times 0.05 = 9.3\ \mu L\,min^{-1}$. In Fig. 3, the first row shows the dynamics when the radius of the longest finger or outermost droplet reached 10 mm, while the second, third, fourth, and final panels correspond to 20, 30, 40, and 50 mm, respectively. The time evolution proceeds from top to bottom for each gap.

In classical Saffman-Taylor instabilities, both fully miscible and immiscible systems exhibit finger-like interfacial patterns [3]. However, partially miscible systems have been reported to form

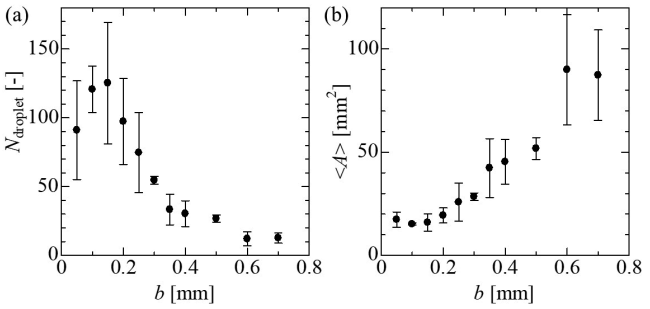


FIG. 4. (a) Number of droplets ($N_{droplet}$) and (b) average droplet size ($<A>$) as functions of gap width ($b$). Error bars represent the standard deviations from three repeated experiments. The plotted data was taken when the radius of the longest finger or outermost droplet reached 50 mm.

multiple droplets instead of distinct fingers [28]. In the present experiments, increasing the gap width led to an increase in droplet size. Several droplets appeared as time progressed. The lighter blue color observed for smaller gaps resulted from the thinner PEG layer, as a larger gap increased the optical thickness, making the color appear darker blue owing to reduced light transmission.

Figure 4 shows the number and average size of the droplets as a function of the gap width. When the gap was small, droplets did not spread isotropically, resulting in significant differences in their numbers and sizes. Moreover, the dye became diluted, blurring the droplet boundaries, making the number and size of smaller droplets difficult to accurately measure. As the gap width increased, the number of droplets decreased, while the average droplet size increased (Fig. 4). Conversely, smaller gaps produced more numerous and smaller droplets, but these often merged during analysis, resulting in an underestimation of their apparent number.

The effect of flow velocity on the displacement dynamics is presented in Fig. 5, where the flow velocity was 186, 372, 930, and 1860 μL min$^{-1}$ mm$^{-1}$, from top to bottom. The number of droplets decreased as the flow velocity increased. At larger gaps ($b \geqslant 0.35$ mm), droplet formation was suppressed, and finger-like structures appeared instead. Consequently, the droplet size increased with increasing flow velocity. This behavior contrasted with that in fully miscible or immiscible

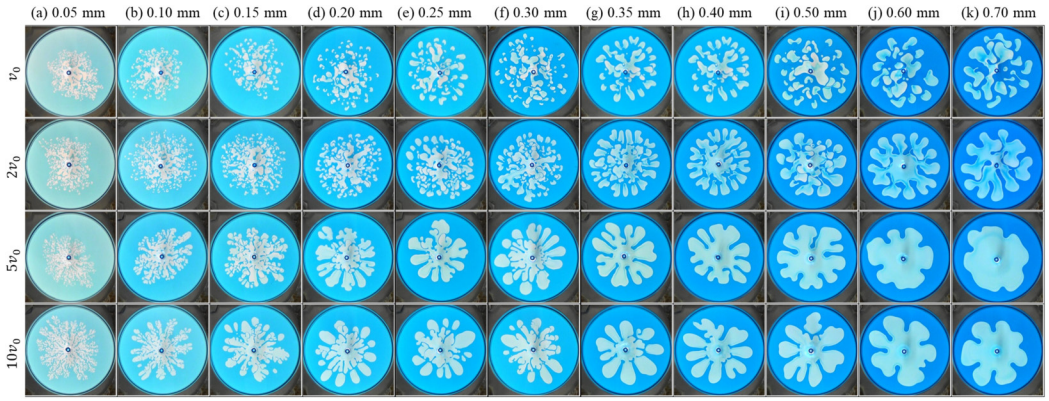


FIG. 5. Fingering dynamics for various flow velocities and gap widths. From left to right, the gap width was (a) 0.05, (b) 0.10, (c) 0.15, (d) 0.20, (e) 0.25, (f) 0.30, (g) 0.35, (h) 0.40, (i) 0.50, (j) 0.60, and (k) 0.70 mm. From top to bottom, the linear flow velocity ($q/b$) was $v_0$, $2v_0$, $5v_0$, and $10v_0$ ($v_0 = 186$ μL min$^{-1}$ mm$^{-1}$). Each image was taken when the radius of the longest finger or outermost droplet reached 50 mm.

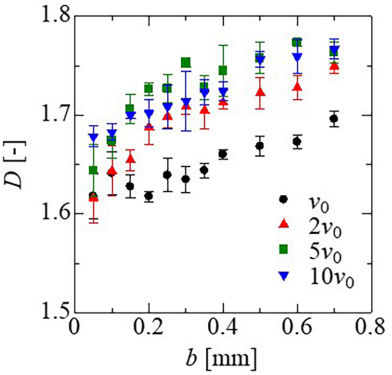


FIG. 6. Relationship between the fractal dimension ($D$) and gap width ($b$). Error bars represent standard deviations from three repeated experiments.

systems, where the finger width decreases or the number of fingers increases as the flow velocity or flow rate increases.

To quantify the interfacial patterns, the fractal dimension ($D$) was measured using the box-counting method [44], which is commonly used for quantitative evaluation of fingering dynamics [45–48]. The fractal dimension provides information regarding the geometrical properties of branched patterns, allowing comparisons among different conditions. The $D$ values were calculated based on binarized images processed with imagej (Fig. 6). The measured $D$ values ranged from 1.6 to 1.8, consistent with literature values for radial viscous fingering [45,46,48,49]. Auerbach and Strobel [49] reported that $D$ approaches 1.7 in the viscous regime (Re $\approx$ 1; Re: Reynolds number) and decreases to 1.5 in the inertia regime (Re $\approx$ 200) for water-glycerol miscible systems. In the present study, the fractal dimension increased with the gap width as droplet formation was suppressed and broader fingers developed. This behavior likely occurred because the fractal dimension was dependent on the covered area of the less viscous solution. This result indicates that hydrodynamic instability became more suppressed as the gap increased. However, this observation differs from that reported in previous literature [49]. In the present study, the Reynolds number (Re $= \rho v r/\mu$) remained constant because the linear velocity ($v$) was fixed, while the gap width varied and both density ($\rho$) and viscosity ($\mu$) were constant. Therefore, the fractal dimension gradually changed even when under constant Re conditions. Although the fractal dimension provides information on hydrodynamic characteristics, it does not reflect chemical or thermodynamic properties. Furthermore, the same trend was observed across different flow velocities. Overall, the $D$ values were smaller at $v_0$ than at $2v_0$, $5v_0$, and $10v_0$. However, no significant difference was observed at a specific $b$ value for different flow velocities, except $v_0$.

We defined randomness ($S$) to quantitatively evaluate the interfacial instability dynamics, and the results are shown in Fig. 7. The randomness parameter $S$ was defined as the number of pixel-to-pixel transitions between black and white along a line scan of the binarized image, normalized by the total number of scanned pixels. In practice, each binary image was scanned pixel by pixel, and every change in pixel value (white to black or black to white) was counted. The value of $S$ was then obtained by dividing this count by the total number of scanned pixels. Preliminary tests confirmed that $S$ is independent of the scanning direction.

$S$, originally defined through image binarization, can also be interpreted from a thermodynamic perspective. A higher $S$ corresponds to a larger interfacial area and stronger concentration gradient, implying enhanced local entropy production. This is because $S$ reflects the spatial heterogeneity of the chemical potential field and can thus be regarded as a measure of entropy production in nonequilibrium interfacial dynamics, since entropy production is defined as $\frac{1}{T}\int J \cdot \nabla \mu dV$, where $T$ is the absolute temperature, $J$ is the mass flux, $\mu$ is the chemical potential, and $V$ is the volume

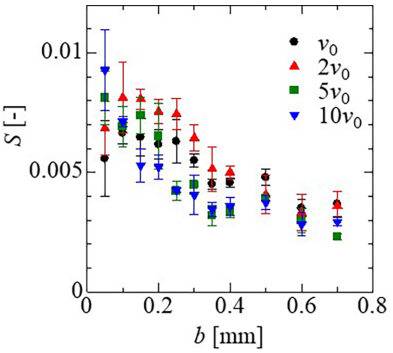


FIG. 7. Randomness ($S$) as a function of gap width ($b$). Error bars represent standard deviations from three repeated experiments. The plotted data was taken when the radius of the longest finger or outermost droplet reached 50 mm.

[29,50,51]. Conversely, a smaller $S$ value reflects an energetically stabilized, ordered interface configuration dominated by interfacial tension. Therefore, $S$ represents a macroscopic manifestation of the competition between hydrodynamic advection and thermodynamic phase separation.

The relationship between $S$ and $b$ is illustrated in Fig. 7. $S$ decreased as the gap increased, indicating that hydrodynamic instability was more suppressed at larger gaps. In the partially miscible PEG-$Na_2SO_4$ system, the decrease in $S$ with increasing gap demonstrates that confinement suppressed thermodynamic instability. Thus, a reduction in $S$ signifies a shift from a thermodynamically driven phase-separation regime (high-entropy interface) to a hydrodynamically stabilized regime (low-entropy interface). This trend remained consistent even when the flow velocity was varied. The randomness parameter $S$ counts the frequency of pixel-level transitions along the interface, reflecting the geometric irregularity owing to hydrodynamic fingering and droplet formation. A decrease in $S$ with increasing gap width therefore indicates smoother interfaces and reduced interfacial complexity, consistent with suppressed hydrodynamic instability. Note that although $S$ and $D$ measure different characteristics—local irregularity and multiscale geometrical complexity, respectively—they both decrease or increase systematically with the suppression of droplet formation. Therefore, while no direct mathematical relationship exists between $S$ and $D$, they exhibit consistent trends because they capture different manifestations of the same physical stabilization process.

We also measured the number of droplets at various flow velocities, as shown in Fig. 8. The flow velocities $v_0$, $2v_0$, $5v_0$, and $10v_0$ correspond to 186, 372, 930, and 1860 $\mu L\,min^{-1}\,mm^{-1}$, respectively. For all flow velocities, the number of droplets decreased as the Hele-Shaw cell gap increased. As the gap widened, the patterns became more hydrodynamically stable, forming thicker and fewer fingers. This behavior is further reinforced by interfacial tension, a characteristic of partially miscible systems. At low injection velocities, numerous droplets formed to maximize the interfacial area. By contrast, at higher injection velocities, the pattern was determined by the balance between interface instability (fingering) caused by injection and droplet formation. Therefore, even at the same gap width, the number of droplets decreased as the flow velocity increased.

The interfacial length of the pattern was analyzed from a chemical thermodynamic perspective. Here, we define the total interfacial length ($I$) as the sum of the perimeters of all droplets and the interfacial lengths of the fingers. $I$ can be interpreted thermodynamically as a measure of interfacial free energy. In partially miscible systems, the evolution of $I$ reflects the competition between the reduction of bulk free energy through phase separation and the increase in interfacial energy due to interface creation. Although the total interfacial length $I$ increases when numerous small droplets are formed, $I$ cannot be expressed solely in terms of the number and size distribution of droplets. This is because the interfacial geometry in the present system includes not only circular droplets

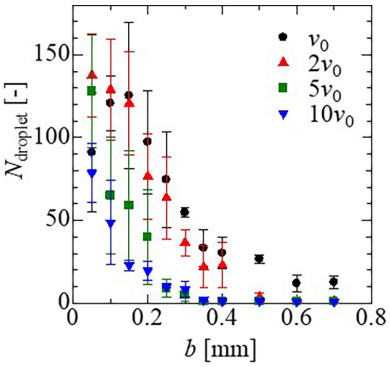


FIG. 8. Number of droplets ($N_{droplet}$) for various flow velocities as a function of gap width ($b$). Error bars represent standard deviations from three repeated experiments. The plotted data was taken when the radius of the longest finger or outermost droplet reached 50 mm.

but also extended finger boundaries generated by the combined effects of hydrodynamic stretching and phase separation. Therefore, $I$ should be regarded as an integrated geometrical measure that incorporates contributions from both droplet interfaces and convoluted finger structures. As a result, changes in droplet number and droplet radius correlate with variations in $I$, but a simple analytical relationship between these quantities does not exist. The trends shown in Figs. 7–9 collectively reflect this mutual but nontrivial dependence.

The observed decrease in $I$ with increasing gap width indicates that geometrical confinement enhanced the thermodynamic driving force toward stable, low-energy configurations. Conversely, the nonmonotonic dependence of $I$ on flow velocity suggests a transition between diffusion-dominated and advection-dominated regimes, where the system explores metastable configurations of higher interfacial energy under nonequilibrium forcing. The dependence of $I$ on the gap width is shown in Fig. 9. The total interfacial length decreased as the gap increased, regardless of the flow velocity. At small gaps, thermodynamic effects dominated over hydrodynamic effects, resulting in numerous droplets and longer interfacial lengths. However, for most gap widths, the interfacial length at $2v_0$ was greater than that at $10v_0$, indicating no correlation between the interfacial length and flow velocity.

Finally, the total interfacial length of the pattern was scaled with the flow velocity, flow rate, and gap width as shown in Fig. 10. The dimensionless parameter $f$ represents a multiple of the

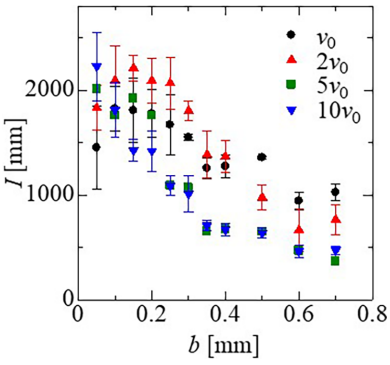


FIG. 9. Total interfacial length ($I$) as a function of gap width ($b$) for various flow velocities. Error bars represent standard deviations from three repeated experiments. The plotted data was taken when the radius of the longest finger or outermost droplet reached 50 mm.

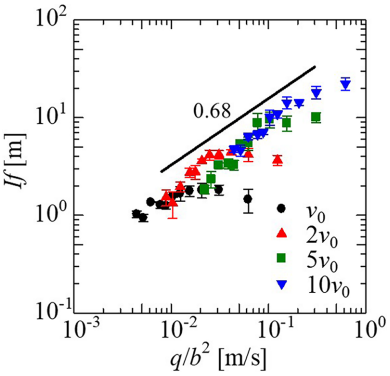


FIG. 10. Scaled interfacial length ($If$) as a function of $q/b^2$. The plotted data was taken when the radius of the longest finger or outermost droplet reached 50 mm.

reference flow velocity ($v_0$). The horizontal axis ($q/b^2$) is a parameter based on Darcy's law for Hele-Shaw flows, reflecting the hydrodynamic effect in this study. The vertical axis represents the scaled interfacial length ($If$), reflecting chemical thermodynamic effects. The scaled interfacial length $If$ was defined as $If = I \times f$, where $I$ is the measured total interfacial length and $f = v/v_0$ is the flow-velocity ratio. In this sense, $If$ represents a hydrodynamically weighted interfacial length. Plotting $If$ against $q/b^2$, which reflects the effective shear rate, allows comparison across different flow velocities and gap widths and reveals the underlying scaling behavior.

As shown in Fig. 10, $If$ is proportional to $(q/b^2)^{0.68}$. Therefore, the total interfacial length is related to the flow velocity ratio $f$, flow rate $q$, and gap $b$. This relationship implies that the observed pattern was due to a balance between chemical thermodynamics and hydrodynamics. Because $I$ reflects the thermodynamic contribution and $q$, $f$, and $b$ are hydrodynamic parameters, the interfacial length can be predicted by the flow rate and gap width. The obtained scaling, $If \propto (q/b^2)^{0.68}$, suggests that the total interfacial length was governed by the competition between thermodynamic interfacial tension, which favored minimizing $I$, and hydrodynamic shear effects, enhanced by increasing $f$ or $q$. The inverse dependence on $b$ indicates that stronger confinement enhanced diffusive mixing and droplet nucleation, effectively increasing interfacial complexity.

The present scaling is based on dimensional quantities without full nondimensionalization (e.g., by capillary number, Péclet number, or Korteweg number). Therefore, the obtained relationship is specific to the PEG-$Na_2SO_4$-water system under room-temperature conditions. However, the scaling exponent is expected to remain similar for other partially miscible systems with comparable interfacial tension and viscosity contrasts.

The experimentally obtained scaling relation, $If \propto (q/b^2)^{0.68}$, can be physically interpreted by considering the balance between interfacial tension and hydrodynamic shear effects in the confined, partially miscible system. In a Hele-Shaw geometry, the characteristic shear rate ($\dot{\gamma}$) is proportional to $q/b^2$, because the local velocity gradient in the gap direction scales as the mean velocity $U \sim q/b$ divided by the gap thickness $b$. Thus, the observed empirical relation can be rewritten as

$$If \propto \dot{\gamma}^{0.68} \sim \dot{\gamma}^{\frac{2}{3}}. \tag{1}$$

This scaling can be derived from a simple force balance between inertial stress and interfacial tension. The interfacial length $If$ represents the total area of newly formed interface and is inversely related to a characteristic domain size ($L$) as $If \sim A/L$, where $A$ is the observation area. Assuming

that the domain size is determined by the condition that inertial and capillary stresses are balanced, i.e., Weber number of order unity (We $= \rho L U^2/\sigma = \rho\dot{\gamma}^2 L^3/\sigma \sim 1$ when $U = \dot{\gamma}L$), we obtain

$$L \sim \left(\frac{\sigma}{\rho\dot{\gamma}^2}\right)^{\frac{1}{3}}, \tag{2}$$

and hence,

$$If \propto \frac{1}{L} \propto \dot{\gamma}^{\frac{2}{3}}. \tag{3}$$

Here, $\rho$ and $\sigma$ denote the fluid density and interfacial tension, respectively. The exponent 2/3 derived from this scaling is in excellent agreement with the experimental value of 0.68, indicating that the interface morphology was governed by competition between capillary relaxation and weak inertial stretching under shear.

By contrast, if the system were entirely in a viscous-capillary regime ($Ca = \mu\dot{\gamma}L/\sigma \sim 1$), the characteristic length would scale as $L \sim \sigma/(\mu\dot{\gamma})$, giving $If \propto \dot{\gamma}$. Alternatively, in a diffusion-controlled regime dominated by Korteweg stresses ($K/L^3 \sim \mu\dot{\gamma}$) [52–54], one would expect $L \sim [K/(\mu\dot{\gamma})]^{1/3}$ and hence $If \propto \dot{\gamma}^{1/3}$. Such viscous-capillary and Korteweg-viscous scaling relations are well established in the theoretical literature on interfacial dynamics and phase ordering. For diffuse interfaces, the Korteweg stress scaling originates from the Cahn Hilliard theory [53], while the associated length-scale evolution in phase-separating systems is discussed comprehensively by Bray [54].

The experimentally observed exponent (0.68) therefore lies between the viscous-capillary and Korteweg-viscous limits but is closer to 2/3, supporting the interpretation that pattern selection occurs in a regime where weak inertia and interfacial tension are balanced. This analysis suggests that the present PEG-$Na_2SO_4$-water system, though nominally at low Reynolds number, operates near a transitional "inertia-modified capillary regime." The scaling law $If \propto (q/b^2)^{0.68}$ therefore arises naturally from the physical constraint We $\sim 1$ under confinement.

## IV. CONCLUSIONS

This study systematically investigated the effects of the gap and flow rate on the displacement of a more viscous fluid by a less viscous one in a Hele-Shaw cell using a partially miscible PEG-$Na_2SO_4$-water system. Compared with fully miscible and immiscible systems, which typically exhibit fingering patterns, the partially miscible system produced multiple droplets.

In this study, we found that the droplet size decreased and the number of droplets increased as the gap width decreased, indicating that the droplet formation intensified under strong confinement. As the flow velocity increased, the number of droplets decreased, and when the gap was sufficiently large ($b \geqslant 0.35$ mm), droplet formation was suppressed and classical fingering reappeared. This behavior contrasted with conventional trends observed in fully miscible and immiscible systems, where increasing flow velocity typically leads to thinner fingers and a greater number of fingers.

The randomness parameter obtained from image binarization decreased with increasing gap width increases, indicating that hydrodynamic instability was suppressed under larger gaps. Similarly, the fractal dimension determined by the box-counting method increased as the gap increased, reflecting the suppression of droplet formation and the development of wide fingers. The total interfacial length decreased with increasing gap at all flow velocities. In addition, a nonmonotonic relationship was observed between the flow velocity and interface length. For instance, the interfacial length was larger at $2v_0$ than at $10v_0$ for several gaps. This may be related to a nonmonotonic behavior of finger width against flow rate due to the balance of interfacial hydrodynamics and chemical thermodynamics [26]. However, numerical simulations should be conducted to completely understand this mechanism—such a challenging issue is left as a future work.

A key finding of this study was the discovery of a scaling law that reflects the balance between inertial stretching and capillary relaxation under geometric confinement. The derived empirical

exponent agreed well with theoretical predictions based on Weber number scaling (We $\sim$ 1), situating the system in a weakly inertial, capillary-dominated regime. This result complements the known viscous-capillary ($If \propto \dot{\gamma}$) and Korteweg-viscous ($If \propto \dot{\gamma}^{1/3}$) limits, establishing a unified framework for pattern selection in partially miscible displacement systems.

The present study demonstrates how the competition between hydrodynamic forcing, geometric confinement, and thermodynamic phase separation governs the onset, suppression, and morphological features of partially miscible viscous fingering. In particular, we identify conditions under which phase-separation-driven droplet formation and interfacial deformation are either enhanced or arrested by the imposed flow. These findings contribute to the growing research trend focusing on the coupling between hydrodynamics and phase separation, especially the flow-induced arrest phenomena that emerge when phase separation occurs within a moving liquid-liquid interfacial region. Such mechanisms directly relate to a methodology for controlling interfacial hydrodynamics via phase separation [55], which has potential applications across a wide range of fields. On the large scale, understanding how flow suppresses or promotes interfacial pattern formation is relevant to enhanced oil recovery [9], $CO_2$ sequestration [56], and the mitigation or manipulation of oil slicks on the ocean surface [57–59]. On the small scale, the ability to modulate interfacial patterns through gap thickness, flow rate, and thermodynamic driving force is useful for the design of microfluidic devices and flow-assisted emulsification technologies where precise control over mixing, dispersion, and morphology is required [60,61].

Furthermore, the aqueous two-phase system (ATPS) used in this study is itself employed in biological and biochemical applications, including the dynamic microcompartmentation of cells, proteins, and nucleic acids [62,63], and it has recently been recognized as a model for membrane-less organelles [64]. The present results—showing how imposed flow can either arrest or promote droplet formation and interfacial structuring—provide a physical framework that may help identify the molecular components, physical properties, and mechanisms underlying intracellular phase separation. Such mechanisms are believed to regulate spatial organization and information processing within membrane-less organelles [65,66].

## ACKNOWLEDGMENTS

The authors thank Masato Shirota for conducting the experiments and image analyses. This study was supported by JST Presto Grant No. JPMJPR22O5.

R.X.S. contributed to the conceptualization, investigation, resources, methodology, software, data curation, formal analysis, funding acquisition, validation, visualization, project administration, original draft writing, review, and editing of this work. Y.N. contributed to the conceptualization, methodology, software, data curation, formal analysis, validation, visualization, and article review and editing of this work. H.M. contributed to the conceptualization, methodology, software, data curation, formal analysis, validation, visualization, and article review and editing of this work.

## DATA AVAILABILITY

The data that support the findings of this article are not publicly available. The data are available from the authors upon reasonable request.

[1] P. G. Saffman and G. Taylor, The penetration of a fluid into a porous medium or Hele-Shaw cell containing a more viscous liquid, Proc. R. Soc. A **245**, 312 (1958).

[2] W. F. Engelberts and L. J. Klinkenberg, Laboratory experiments on the displacement of oil by water from packs of granular material, World Pet. Congr. **544** (1951).

[3] G. M. Homsy, Viscous fingering in porous media, Annu Rev Fluid Mech **19**, 271 (1987).

[4] H. S. Hele-Shaw, The flow of water, Nature (London) **58**, 34 (1898).
[5] H. P. G. Darcy, *Les Fontaines Publiques de La Ville de Dijon* (Victor Dalmont, Paris, 1856).
[6] K. J. Mayfield, R. A. Shalliker, H. J. Catchpoole, A. P. Sweeney, V. Wong, and G. Guiochon, Viscous fingering induced flow instability in multidimensional liquid chromatography, J. Chromatogr. A **1080**, 124 (2005).
[7] K. R. Bhaskar, P. Garik, B. S. Turner, J. D. Bradley, R. Bansil, H. E. Stanley, and J. T. LaMont, Viscous fingering of HCl through gastric mucin, Nature (London) **360**, 458 (1992).
[8] J. A. Pojman, G. Gunn, C. Patterson, J. Owens, and C. Simmons, Frontal dispersion polymerization, J. Phys. Chem. B **102**, 3927 (1998).
[9] L. W. Lake, R. T. Johns, W. R. Rossen, and G. A. Pope, *Fundamentals of Enhanced Oil Recovery* (Society of Petroleum Engineers, Richardson, 2014).
[10] T. T. Al-Housseiny, P. A. Tsai, and H. A. Stone, Control of interfacial instabilities using flow geometry, Nat. Phys. **8**, 747 (2012).
[11] T. T. Al-Housseiny and H. A. Stone, Controlling viscous fingering in tapered Hele-Shaw cells, Phys. Fluids **25**, 092102 (2013).
[12] Z. Zheng, H. Kim, and H. A. Stone, Controlling viscous fingering using time-dependent strategies, Phys. Rev. Lett. **115**, 174501 (2015).
[13] G. Bongrand and P. A. Tsai, Manipulation of viscous fingering in a radially tapered cell geometry, Phys. Rev. E **97**, 061101(R) (2018).
[14] S. Nand, V. Sharma, S. K. Das, S. S. Padhee, and M. Mishra, Effect of Hele–Shaw cell gap on radial viscous fingering, Sci. Rep. **12**, 18967 (2022).
[15] Z. Wang, J. M. Pereira, E. Sauret, and Y. Gan, Emergence of unstable invasion during imbibition in regular porous media, J. Fluid Mech. **941**, A40 (2022).
[16] T. Pak, H. S. Rabbani, A. Q. Raeini, and N. Shokri, Effects of the pore morphology on multiphase fluid displacement in porous media–a high-resolution modeling investigation, ACS Omega **8**, 3889 (2023).
[17] K. Osei-Bonsu, P. Grassia, and N. Shokri, Effects of pore geometry on flowing foam dynamics in 3D-printed porous media, Transp. Porous Media **124**, 903 (2018).
[18] S. Bakhshian, S. A. Hosseini, and N. Shokri, Pore-scale characteristics of multiphase flow in heterogeneous porous media using the lattice Boltzmann method, Sci. Rep. **9**, 3377 (2019).
[19] D. S. Wu, R. Hu, T. Lan, and Y. F. Chen, Role of pore-scale disorder in fluid displacement: Experiments and theoretical model, Water Resour. Res. **57**, e2020WR028004 (2021).
[20] L. Xiao and J. Yao, Effects of heterogeneity of porous media and wettability on forced imbibition, IOP Conf. Ser. Earth Environ. Sci. **657**, 012051 (2021).
[21] F. J. Meigel, T. Darwent, L. Bastin, L. Goehring, and K. Alim, Dispersive transport dynamics in porous media emerge from local correlations, Nat. Commun. **13**, 5885 (2022).
[22] X. Fu, L. Cueto-Felgueroso, and R. Juanes, Thermodynamic coarsening arrested by viscous fingering in partially miscible binary mixtures, Phys. Rev. E **94**, 033111 (2016).
[23] X. Fu, L. Cueto-Felgueroso, and R. Juanes, Viscous fingering with partially miscible fluids, Phys. Rev. Fluids **2**, 104001 (2017).
[24] L. Palodhi, M. C. Kim, and M. Mishra, Trade off between hydrodynamic and thermodynamic forces at the liquid-liquid interface, Langmuir **40**, 7595 (2024).
[25] Y. F. Deki, R. X. Suzuki, C. C. Chou, T. Ban, M. Mishra, Y. Nagatsu, and C. Y. Chen, Numerical simulation of effects of phase separation on viscous fingering in radial Hele-Shaw flows, J. Fluid Mech. **1003**, A12 (2025).
[26] R. X. Suzuki, T. Ban, M. Mishra, and Y. Nagatsu, Pattern transitions and nonmonotonic changes in finger width due to the flow rate in partially miscible viscous fingering, Phys. Rev. E **112**, 025104 (2025).
[27] M. A. Amooie, M. R. Soltanian, and J. Moortgat, Hydrothermodynamic mixing of fluids across phases in porous media, Geophys. Res. Lett. **44**, 3624 (2017).
[28] R. X. Suzuki, Y. Nagatsu, M. Mishra, and T. Ban, Phase separation effects on a partially miscible viscous fingering dynamics, J. Fluid Mech. **898**, A11 (2020).
[29] R. X. Suzuki, S. Kobayashi, Y. Nagatsu, and T. Ban, Tunable hydrodynamic interfacial instability by

controlling a thermodynamic parameter of liquid–liquid phase separation, J. Phys. Chem. B **125**, 7508 (2021).
[30] R. X. Suzuki, H. Tada, S. Hirano, T. Ban, M. Mishra, R. Takeda, and Y. Nagatsu, Anomalous patterns of Saffman-Taylor fingering instability during a metastable phase separation, Phys. Chem. Chem. Phys. **23**, 10926 (2021).
[31] S. Seya, R. X. Suzuki, Y. Nagatsu, T. Ban, and M. Mishra, Numerical study on topological change of viscous fingering induced by a phase separation with Korteweg force, J. Fluid Mech. **938**, A18 (2022).
[32] K. Iwasaki, Y. Nagatsu, T. Ban, J. Iijima, M. Mishra, and R. X. Suzuki, Experimental demonstration of the suppression of viscous fingering in a partially miscible system, Phys. Chem. Chem. Phys. **25**, 13399 (2023).
[33] M. C. Kim, L. Palodhi, J. S. Hong, and M. Mishra, Effect of thermodynamic instability on viscous fingering of binary mixtures in a Hele-Shaw cell, J. Fluid Mech. **972**, A23 (2023).
[34] R. X. Suzuki, S. Seya, T. Ban, M. Mishra, and Y. Nagatsu, Arresting of interfacial phase separation with an imposed flow, Phys. Rev. Fluids **9**, 024003 (2024).
[35] N. Vladimirova, A. Malagoli, and R. Mauri, Diffusiophoresis of two-dimensional liquid droplets in a phase-separating system, Phys. Rev. E **60**, 2037 (1999).
[36] D. Molin, R. Mauri, and V. Tricoli, Experimental evidence of the motion of a single out-of-equilibrium drop, Langmuir **23**, 7459 (2007).
[37] P. Poesio, G. P. Beretta, and T. Thorsen, Dissolution of a liquid microdroplet in a nonideal liquid-liquid mixture far from thermodynamic equilibrium, Phys. Rev. Lett. **103**, 064501 (2009).
[38] T. Ban, A. Aoyama, and T. Matsumoto, Self-generated motion of droplets induced by Korteweg force, Chem. Lett. **39**, 1294 (2010).
[39] T. Ban, T. Yamada, A. Aoyama, Y. Takagi, and Y. Okano, Composition-dependent shape changes of self-propelled droplets in a phase-separating system, Soft Matter **8**, 3908 (2012).
[40] T. Ban, T. Fukuyama, S. Makino, E. Nawa, and Y. Nagatsu, Self-propelled vesicles induced by the mixing of two polymeric aqueous solutions through a vesicle membrane far from equilibrium, Langmuir **32**, 2574 (2016).
[41] S. M. Snyder, K. D. Cole, and D. C. Sziag, Phase compositions, viscosities, and densities for aqueous two-phase systems composed of polyethylene glycol and various salts at 25°C, J. Chem. Eng. Data **37**, 268 (1992).
[42] R. X. Suzuki, R. Takeda, Y. Nagatsu, M. Mishra, and T. Ban, Fluid morphologies governed by the competition of viscous dissipation and phase separation in a radial Hele-Shaw flow, Coatings **10**, 960 (2020).
[43] R. X. Suzuki, Y. Nagatsu, M. Mishra, and T. Ban, Fingering pattern induced by spinodal decomposition in hydrodynamically stable displacement in a partially miscible system, Phys. Rev. Fluids **4**, 104005 (2019).
[44] P. Grassberger, On the fractal dimension of the Henon attractor, Phys. Lett. A **97**, 224 (1983).
[45] S. E. May and J. V. Maher, Fractal dimension of radial fingering patterns, Phys. Rev. A **40**, 1723 (1989).
[46] J. D. Chen, Growth of radial viscous fingers in a Hele-Shaw cell, J. Fluid Mech. **201**, 223 (1989).
[47] K. V. McCloud and J. V. Maher, Experimental perturbations to Saffman-Taylor flow, Phys. Rep. **260**, 139 (1995).
[48] O. Praud and H. L. Swinney, Fractal dimension and unscreened angles measured for radial viscous fingering, Phys. Rev. E **72**, 011406 (2005).
[49] D. Auerbach and G. Strobel, Fingering patterns and their fractal dimensions, Chaos Solitons Fractals **5**, 1765 (1995).
[50] S. R. De Groot and P. Mazur, *Non-Equilibrium Thermodynamics* (Dover, New York, 1984).
[51] S. Kjelstrup, D. Bedeaux, A. Hansen, B. Hafskjold, and O. Galteland, Non-isothermal transport of multi-phase fluids in porous media, The entropy production, Front. Phys. **6**, 126 (2018).
[52] D. J. Korteweg, Sur La Forme Que Prennent Les Équations Du Mouvement Des Fluides Si l'on Tient Compte Des Forces Capillaires Caușees Par Des Variations de Densité Considérables Mais Continues et Sur La Théorie de La Capillarité Dans l'hypothèse d'une Variation Continue D, Arch. Néerl. Sci. Exactes Nat. **6**, 1 (1901).

[53] J. W. Cahn and J. E. Hilliard, Free energy of a nonuniform system, I. Interfacial free energy, J. Chem. Phys. **28**, 258 (1958).
[54] A. J. Bray, Theory of phase-ordering kinetics, Adv. Phys. **43**, 357 (1994).
[55] T. Ban, Y. Kobayashi, R. Suzuki, and Y. Nagatsu, Active liquid matter driven by nonequilibrium interfacial tension, J. Phys. Soc. Japan **86**, 101005 (2017).
[56] F. M. J. Orr and J. J. Taber, Use of carbon dioxide in enhanced oil recovery, Science **224**, 563 (1984).
[57] M. Reed, O. Johansen, P. J. Brandvik, P. Daling, A. Lewis, R. Fiocco, D. Mackay, and R. Prentki, Oil spill modeling towards the close of the 20th century: Overview of the state of the art, Spill Sci. Technol. Bullentin **5**, 3 (1999).
[58] S. D. Wang, Y. M. Shen, and Y. H. Zheng, Two-dimensional numerical simulation for transport and fate of oil spills in seas, Ocean Eng. **32**, 1556 (2005).
[59] M. J. Olascoaga and G. Haller, Forecasting sudden changes in environmental pollution patterns, Proc. Natl. Acad. Sci. USA **109**, 4738 (2012).
[60] H. A. Stone, A. D. Stroock, and A. Ajdari, Engineering flows in small devices, Annu Rev Fluid Mech **36**, 381 (2004).
[61] G. M. Whitesides, The origins and the future of microfluidics, Nature (London) **442**, 368 (2006).
[62] M. S. Long, C. D. Jones, M. R. Helfrich, L. K. Mangeney-Slavin, and C. D. Keating, Dynamic microcompartmentation in synthetic cells, Proc. Natl Acad. Sci. USA **102**, 5920 (2005).
[63] H. Tavana, A. Jovic, B. Mosadegh, Q. Y. Lee, X. Liu, K. E. Luker, G. D. Luker, S. J. Weiss, and S. Takayama, Nanolitre liquid patterning in aqueous environments for spatially defined reagent delivery to mammalian cells, Nat. Mater. **8**, 736 (2009).
[64] B. Y. Zaslavsky, L. A. Ferreira, A. L. Darling, and V. N. Uversky, The solvent side of proteinaceous membrane-less organelles in light of aqueous two-phase systems, Int. J. Biol. Macromol. **117**, 1224 (2018).
[65] P. Li, S. Banjade, H. C. Cheng, S. Kim, B. Chen, L. Guo, M. Llaguno, J. V. Hollingsworth, D. S. King, S. F. Banani, P. S. Russo, Q. X. Jiang, B. T. Nixon, and M. K. Rosen, Phase transitions in the assembly of multivalent signalling proteins, Nature (London) **483**, 336 (2012).
[66] C. P. Brangwynne, P. Tompa, and R. V. Pappu, Polymer physics of intracellular phase transitions, Nat. Phys. **11**, 899 (2015).